CHAPTER XII *PHASE TRANSFORMATIONS II: SOLID STATE TRANSFORMATIONS*

12.1 Introduction

The previous chapter dealt with the thermodynamic formalism of phase transformations and details specific to the solidification process. This chapter primarily discusses transformations in the solid state in two principal categories: diffusion-mediated transformations and diffusionless cooperative transitions.

Any phase transformation, regardless of whether it is a state transition (e.g., solidification, melting) or a solid-state transformation (e.g., allotropic transformation, precipitation, martensitic transformation), occurs by a rearrangement of atoms, ions, or molecules that starts from a metastable state and then reaches a lower energy state. Such state and phase transitions require overcoming an activation barrier to initiate the phase transformation, typically accomplished by thermal activation or applied stress. After overcoming this barrier, the difference in free energy between the metastable and the lower-energy (more stable) final state drives the transformation.

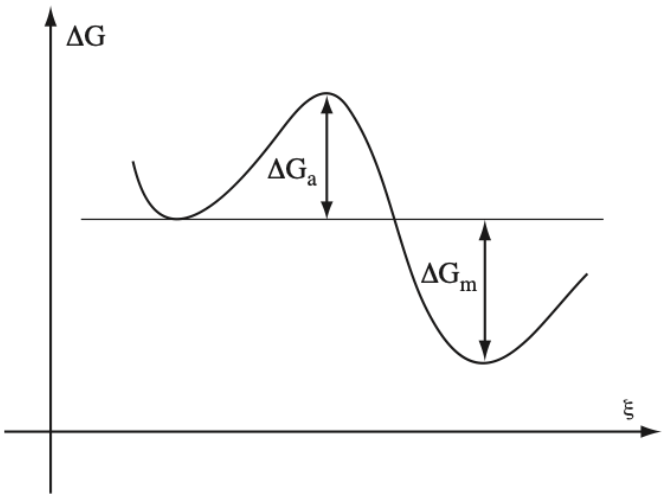

By representing the variations in free energy as a function of a parameter ξ (internal variable), which allows for characterizing the different phases (for example, an interatomic distance), we note that these two quantities are essential in a phase transformation:

$\Delta G_m =$ driving force of the reaction, and the
$\Delta G_a =$ activation energy of the process

Figure 12-1: *Diagram showing the potential barrier to a generic phase transformation*

The formalism applied to solid-state transformations is similar to that developed for solidification. The main difference lies in the volume variations or crystallographic changes between the parent phase and the solid nucleus, often leading to internal elastic stresses. Otherwise, as in the case of solidification theory, we can differentiate between two kinds of nucleation.

General nucleation (or *homogeneous* nucleation) leads to a uniform distribution of nuclei throughout the volume. In contrast, *localized germination* (or *heterogeneous*) promotes nucleation in some sites more than others, such as grain boundaries or dislocations.

The growth of these nuclei can be thermally activated or not (martensitic type). The thermally activated growth of a phase is generally regulated by diffusion. We can set apart:

- Transformations resulting from long-range diffusion, e.g., precipitation and eutectoid transformations.
- Transformations with short-range diffusion (e.g., across habit plane interface): allotropic transformations, order-disorder, etc.

12.2 Transformations with diffusion

12.2.1 Homogeneous nucleation

For simplicity, in this section, we consider the nucleation of a phase β rich in atoms of type B in a matrix phase α rich in atoms of type A. As in solidification, an interface must form during nucleation, which requires energy. This energy contributes to the height of the potential barrier. This energy depends on the surface created S and the surface tension γ. In addition, we must add the elastic energy ΔG_{el} due to the elastic misfit between the parent phase (m) and the daughter phase (c).

This energy, calculated per unit volume, is essentially (7.16):

$$\frac{1}{2}\sigma\varepsilon \propto \mu\varepsilon^2$$

The sum of these contributions, with the driving force of the transformation $V(g_c - g_m) = V\Delta g_V$ gives the variation in free energy:

$$\Delta G_{hom} = V(\Delta g_V + \Delta g_{el}) + S\gamma \tag{12.1}$$

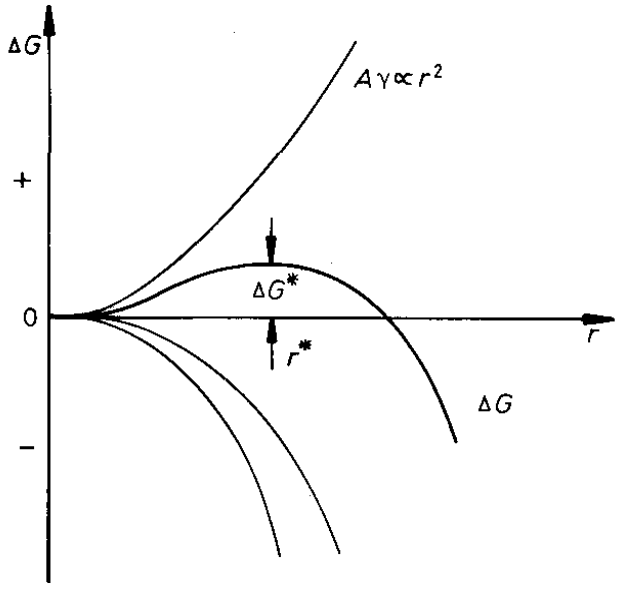

Figure 12-2: *Critical radius of nucleation*

In the case of a spherical precipitate with a radius of r, we get:

$$\Delta G_{hom} = \frac{4}{3}\pi r^3(\Delta g_V + \Delta g_{el}) + 4\pi r^2\gamma \tag{12.2}$$

From this relation, we can deduce the critical growth radius of the nucleus:

$$r^*_{hom} = \frac{-2\gamma}{(\Delta g_V + \Delta g_{el})} \tag{12.3}$$

and the free energy corresponding to the potential barrier is:

$$\Delta G^*_{hom} = \frac{16\pi\gamma^3}{3}\frac{1}{(\Delta g_V + \Delta g_{el})^2} \tag{12.4}$$

Homogeneous nucleation rate

We define the nucleation rate assuming the same arguments used for solidification in Chapter XI. Thus, as in § 11.4.2, the nucleation rate can be expressed as:

$$I_{hom} = I_{0,\text{hom}} e^{-\frac{\Delta G^*_{hom} + \Delta G^S}{kT}} \tag{12.5}$$

where ΔG^S is the diffusion energy.

The effect of the two terms of the activation energy is shown in Figure 12-3.

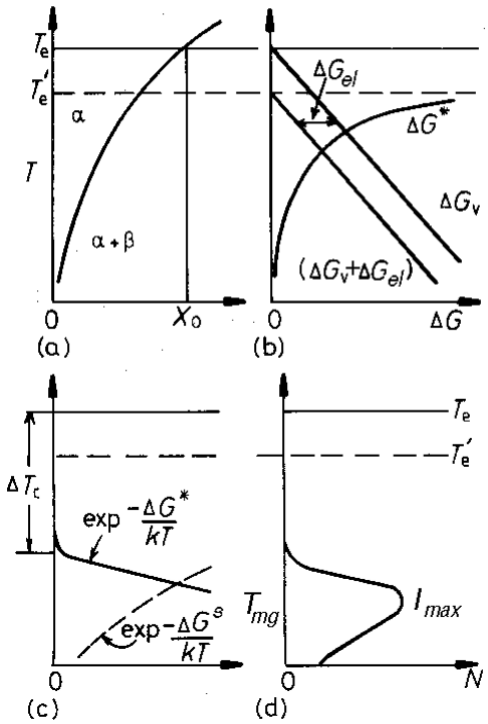

Figure 12-3: *Thermal activation of the nucleation rate*

Supposing that the chemical driving force (Δg_v) varies linearly with temperature (as in equation (11.35)), whereas Δg_{el} stays constant, equation (12.4) implies that the potential barrier ΔG^* varies quadratically with temperature (Figure 12-3b). Thus, at a temperature close to /, the exponential term regulates the nucleation rate, e.g., $\exp\left(\left(-\Delta G^*\right)/\left(kT\right)\right)$.

When the temperature decreases, diffusion is regulated by the activation energy ΔG^S is limited, and this exponential term becomes roughly $\exp\left(\left(-\Delta G^*\right)/\left(kT\right)\right) \sim 1$. As a result, the nucleation is dominated by the term $\exp\left(\left(-\Delta G^S\right)/\left(kT\right)\right)$. Thus, the nucleation rate passes through a maximum at the temperature T_{mg} (Figure 12-3d). Interestingly, nucleation cannot begin until $T_e' < T_e$, where $\Delta G^* \to \infty$.

Using (11.35) and replacing the melting point with the equilibrium temperature between the two phases T_e in that equation. If $\Delta G^* \to \infty$ and $\Delta s(T - T_e) + \Delta g_{el} = 0$ then $T_e' = -\Delta g_{el} + \Delta s T_e$.

Homogeneous nucleation is - in reality - very rare in solids since the difference in structure between the parent phase and the daughter phase makes the term Δg_{el} very large. However, we can observe homogeneous nucleation leading to the formation of coherent precipitates.

a) Example of homogeneous nucleation: Guinier-Preston zones

Let's consider the example of the alloy Al-Ag. Its phase diagram is shown in Figure 12-4. The equilibrium of an Al-Ag 6% atomic (~20% weight) phase is realized at atmospheric pressure and:

- At 500˚C, by one only phase α_{Al} with FCC structure, containing only 6% at. of Ag
- At 300˚C, by a mixture of two phases: α_{Al} with FCC structure, containing 0.8 % of atoms of Ag, and γ with HC structure, containing 59 % of atoms of Ag.

The lever rule can calculate the proportion of each phase applied to the phase diagram in Figure 12-4:

$$X_{\alpha_{Al}} = \frac{59-6}{59-0.8} = 91\% \quad \text{and} \quad X_\gamma = 1 - X_{\alpha_{Al}} = 9\%$$

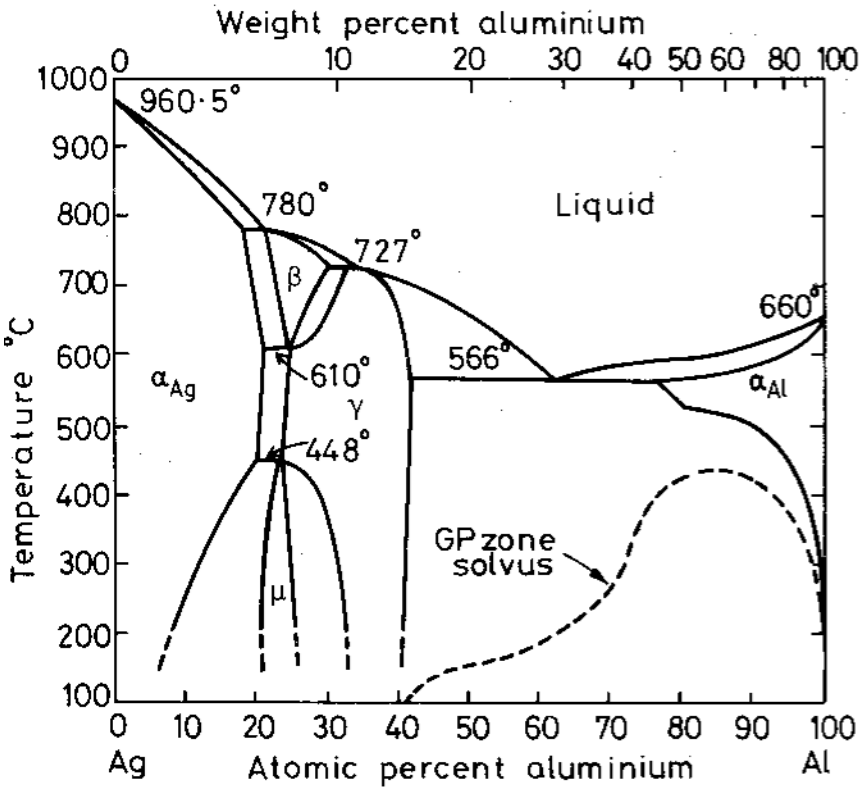

Figure 12-4: *Phase diagram of Al-Ag*

The alloy does not evolve at equilibrium if the temperature variations are infinitely slow. However, in the two-phase state (α+γ), it is possible to monitor γ dissolution during the slow increase in temperature up to 500˚C, e.g., by measuring electrical resistivity (Figure 12-5).

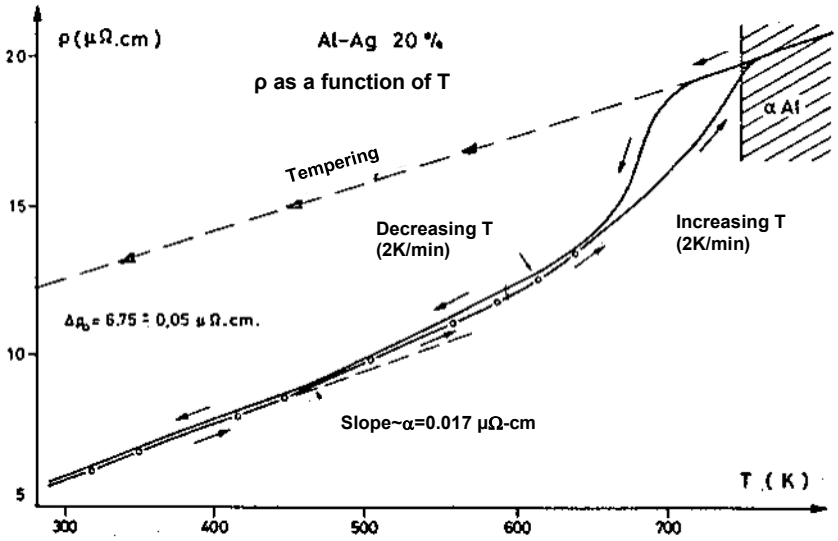

Figure 12-5: *Electrical resistivity as a function of temperature in an Al-Ag 20% alloy*

We observe an increase in the residual electrical resistivity ρ_0 due to the enrichment of the solid solution α_{Al} with Ag atoms during the dissolution of the phase γ (Matthiessen rule: $\rho(T) = \rho_0 + \alpha T$, where $\rho_0 = \rho_0(C)$, equation (4.44)). We do not observe the prior resistivity when the alloy is rapidly cooled by water quenching. Instead, an excess of residual electrical resistivity is measured: $\Delta\rho_0$. The alloy is unstable, i.e., in a non-equilibrium state, and evolves with time, and the phase $\alpha(Al)$ is oversaturated with Ag atoms, e.g., an oversaturated solid solution $\alpha_{Al_{SS}}$. Returning to the equilibrium state requires the formation of precipitates of the phase γ, which is richer in Ag than α_{Al} and requires the thermally activated diffusion of Ag atoms. That is, thermal energy must be supplied to cause the alloy to evolve, a process known as annealing.

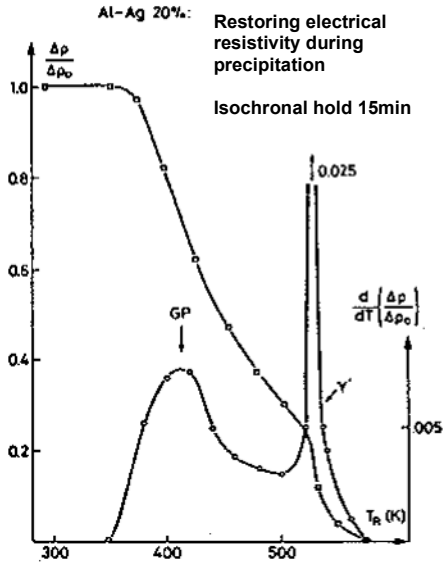

Figure 12-6: *Recovery of the electrical resistivity during isochronous annealings at room temperature*

It is possible to follow the precipitation and formation of phase γ by measuring the recovery of the excess electrical resistivity during annealing, which typically decreases resistivity. The resulting slope changes mark precipitation events (Figure 12-6). For example, this recovery is characterized by two "precipitation stages" that correspond to metastable equilibrium states of the alloy. By transmission electron microscopy and by quenching the metal at each precipitation event, it is possible to observe the initiation of each precipitation stage and phase, as well as the morphology of metastable precipitates (Figure 12-7).

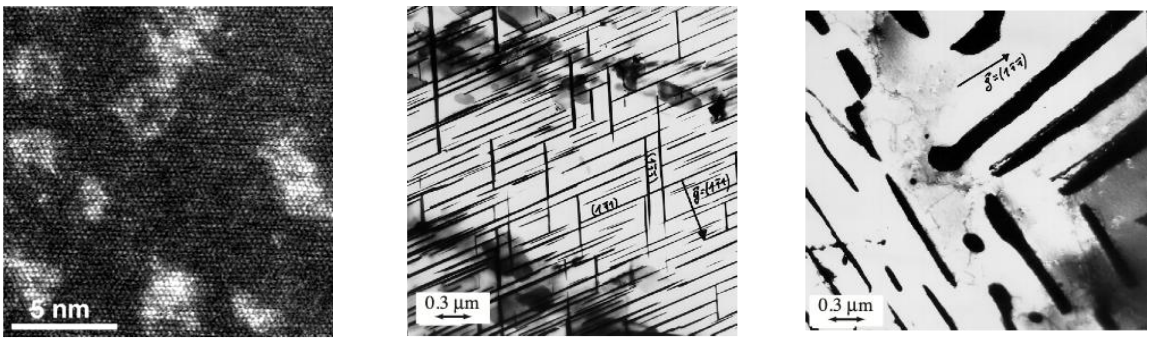

Figure 12-7: *3 kinds of precipitates appear during the precipitation of Al-Ag 20%: Guinier-Preston (a), γ (b), and γ (c)*

The precipitation sequence of the alloy Al-Ag, starting from an oversaturated solid solution $\alpha_{Al_{SS}}$ obtained by quenching, is the following:

$$\alpha_{Al_{SS}} \rightarrow \text{GP zones} \rightarrow \gamma' \rightarrow \gamma$$

- The GP zones are the Guinier-Preston zones comprising spherical clusters, rich in Ag atoms, some tens of nanometers in size, with FCC structure and coherent with the matrix (Figure 12-7a). Being coherent and having a different crystal structure, they strengthen the material by providing barriers to matrix dislocation motion, thereby increasing yield strength.
- The γ' precipitates (Figure 12-7b) appear as thin, flat layers in epitaxial correspondence with the (111) planes of the matrix. Their structure is hexagonal (HC), and their composition is close to Ag_2Al. They have a coherent interface between their base planes (0001) and (111) matrix planes. Also, because they are coherent and have a different crystal structure, these precipitates strengthen the material by impeding dislocation motion (the precipitate cutting bypass mechanism).
- The γ precipitates are the stable form of the phase γ (HC, Ag_2Al). They are incoherent (no continuity between their crystallographic planes and the matrix). Therefore, they tend to appear first at the grain boundaries (Figure 12-7c).

Why these stages of precipitation?

Even if the free energy of the phase γ is the lowest, the potential barrier for its formation is too high. Thus, the system prefers" to go through the intermediate stages, each characterized by lower activation energy. Therefore, we first have the formation of those precipitates that cause the least elastic misfit: the GP zones, which are coherent precipitates with the same structure as the matrix. Then, we have semi-coherent precipitates γ' and, finally, stable precipitates γ. The GP zones are formed by uniform nucleation, whereas the phases γ and γ' are formed on preferential sites, giving way to heterogeneous nucleation. The enrichment forms the γ' precipitates with Ag of the stacking faults formed in the aluminum by dissociating into Shockley partial dislocations. These (see § 7.6.1) are already nuclei of the HC phase as the γ' phase. The γ phase can be formed either from the γ' phase or on the grain boundaries with cellular growth. This last mechanism leads to microstructures very similar to those observed in perlite growth. In the case of Al-Ag alloys, we would observe the decomposition into the α+γ phases. Diffusion through the matrix is replaced by diffusion in the grain boundary, which is faster. The grain boundary moves together with the cell growth.

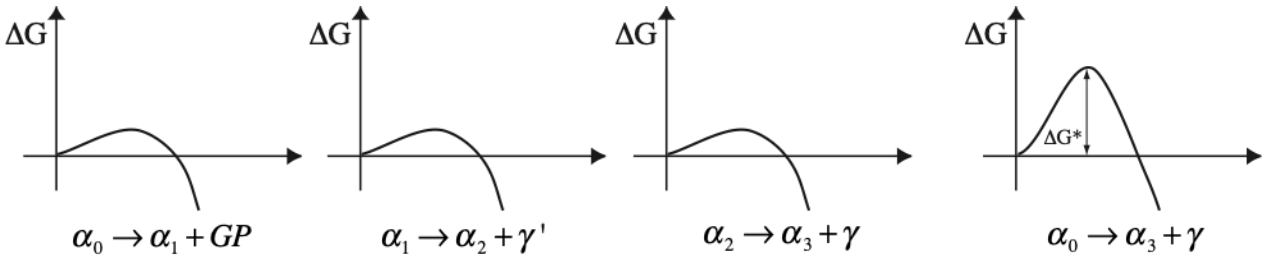

Figure 12-8: *The activation energy for the formation of each transition is minimal compared to the barrier to the direct formation of the stable γ phase.*

12.2.2 Heterogeneous nucleation

In the previous paragraphs, we hinted that heterogeneous nucleation is characterized by the presence of preferential sites, such as dislocations or grain boundaries, i.e., the presence of local defects.
Since it is generally more energetically favorable due to the nucleation on defects, heterogeneous nucleation tends to be the most common form for solid-state transformations in materials. If we assume the creation of a nucleus as the annihilation of a defect, we gain in energy by ΔG_d and equation (12.1) becomes:

$$\Delta G_{het} = V(\Delta g_V + \Delta g_{el}) + S\gamma - \Delta G_d \tag{12.6}$$

For instance, in the case of nucleation at grain boundaries, a nucleus is favorable if it reduces the interface energy between two grains.

$$\Delta G_{het} = V(\Delta g_V + \Delta g_{el}) + S_{\alpha\beta}\gamma_{\alpha\beta} - S_{\alpha\alpha}\gamma_{\alpha\alpha} = V(\Delta g_V + \Delta g_{el}) + S\gamma_{\alpha\beta} - \Delta G_d \tag{12.7}$$

where $S_{\alpha\beta}\gamma_{\alpha\beta}$ corresponds to the energy for the creation of a new interface αβ and $S_{\alpha\alpha}\gamma_{\alpha\alpha}$ corresponds to the energy lost by the suppression of part of the grain boundary αα (Figure 12-9).

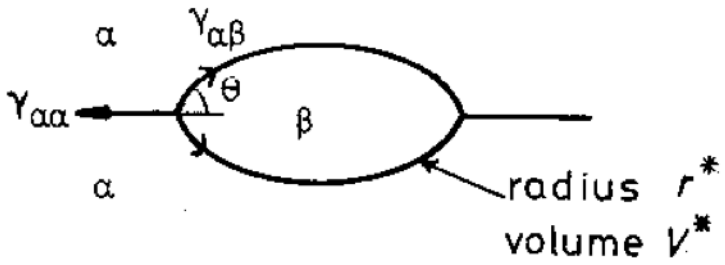

Figure 12-9: *Surface energy of a nucleus developing at the interface between two grain boundaries*

Equations (12.6) and (12.7) are similar but include S terms representing the portion of the αα surface that has not yet been affected by the nucleus. In this formalism, we can then provide an identical calculation for forming a solid nucleus on a surface (see equation (11.40)). However, we write it in terms of Young s law is written $\cos\theta = \frac{\gamma_{\alpha\alpha}}{2\gamma_{\alpha\beta}}$, and obtain the following:

$$r^*_{het} = \frac{-2\gamma_{\alpha\beta}}{\Delta g_V + \Delta g_{el}} \tag{12.8}$$

$$\Delta G^*_{het} = \frac{16\pi}{3}\frac{\gamma^3_{\alpha\beta}}{(\Delta g_V + \Delta g_{el})^2}\frac{(2 - 3\cos\theta + (cos\theta)^3)}{2} \tag{12.9}$$

This result differs by a factor of 2 from the result obtained for solidification in (11.42). Thus, comparing (12.9) and (12.4), we get the following:

$$\frac{\Delta G^*_{het}}{\Delta G^*_{hom}} = \frac{(2 - 3\cos\theta + (cos\theta)^3)}{2} = S(\theta) \tag{12.10}$$

As $\cos\theta = \frac{\gamma_{\alpha\alpha}}{2\gamma_{\alpha\beta}}$, if the interface energy ratio $\frac{\gamma_{\alpha\alpha}}{\gamma_{\alpha\beta}} > 2$, then $\theta = 0$, there is no barrier to the heterogeneous nucleation process anymore. In intermediate situations, the function $S(\theta)$ determines whether nucleation at the grain boundaries is favorable.

Heterogeneous nucleation rate

As for homogeneous nucleation, we can define a heterogeneous nucleation rate:

$$I_{het} = I_{0,het} e^{-\frac{\Delta G^*_{het} + \Delta G^S}{kT}} \tag{12.11}$$

Thus:

$$\frac{I_{het}}{I_{hom}} = \frac{I_{0,het}}{I_{0,hom}} e^{\frac{\Delta G^*_{hom} - \Delta G^*_{het}}{kT}} \tag{12.12}$$

We neglect possible differences in the diffusion energy between the preferential sites and the matrix. In homogeneous nucleation, each atom is a potential nucleation site. Thus, if we consider the nucleation at the grain boundaries, the ratio $\frac{I_{0,het}}{I_{0,hom}} \approx \frac{\delta}{D}$ where δ is the thickness of the interface, and D is the size of the grains. For example, by letting the grain size be 5 μm with a thickness at the grain boundaries of 0.5 nm, we have $\frac{\delta}{D} = 10^{-4}$. Thus, the difference in the nucleation barriers $\Delta G^*_{hom} - \Delta G^*_{het}$ justifies an exponential factor of the same order of magnitude.

Remark

The equations modeling the precipitate growth are similar to those describing solidification. Thus, precipitation kinetics can be determined and described in TTT diagrams, as discussed in § 11.4.3.

12.3 Transformation kinetics: Avrami-Johnson-Mehl equation

The kinetics for nucleation and growth during an isothermal transformation can be characterized phenomenologically by measuring the transformed phase fraction, *f*, as a function of time. This quantity ranges from 0 (no nuclei) to 1 (fully transformed). Many factors determine the phase fraction, f, such as the nucleation rate, nucleation type, and growth rate. Thus, we can imagine that the nucleation occurs during all the transformation stages. In this case, the transformation is solely controlled by nucleation and growth rates. If, on the contrary, all nuclei are created at the beginning of the transformation, only the growth rate governs the transformation. For transformations forming cellular microstructures (§ 12.2.1a), the formation of daughter phases consumes the parent phases, and cell overlap limits the transformation. In the following model, we suppose the nucleation rate *I* is constant. If the cells have a spherical shape and grow at a velocity (*v*) also assumed constant, the volume of a cell nucleated at $t = 0$ is the following:

$$V_c = \frac{4\pi}{3} r^3 = \frac{4\pi}{3} (vt)^3 \tag{12.13}$$

A cell nucleated at t = τ has a volume:

$$\bar{V}_c = \frac{4\pi}{3} v^3 (t-\tau)^3 \tag{12.14}$$

The number of cells forming per unit volume between $t = 0$ and $t = d\tau$ is $N = I\, d\tau$, and thus, if there is no overlap between the growing nuclei, the total transformed volume is given by:

$$V_t = \sum \bar{V}_c = \frac{4\pi}{3} I v^3 \int_0^t (t-\tau)^3 d\tau \tag{12.15}$$

and by integrating, we find:

$$V_t = \frac{\pi}{3} I v^3 t^4 \tag{12.16}$$

This is valid for small volume fractions, where we can neglect overlap. We use the trick illustrated in Figure 12-10 to calculate what happens over long time intervals.

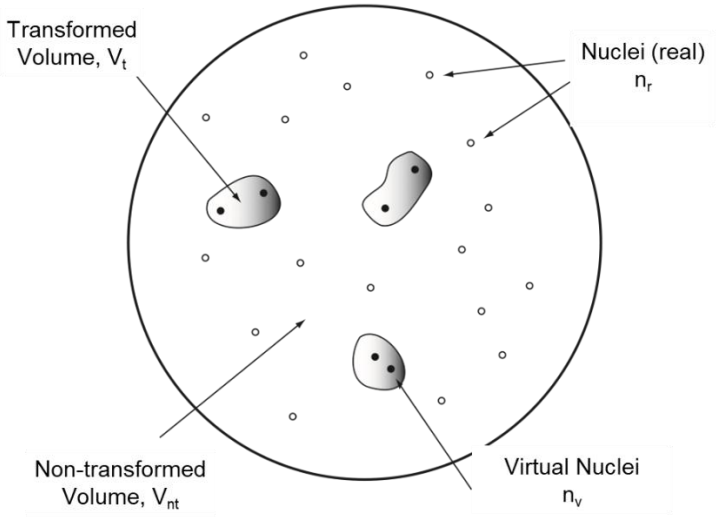

Figure 12-10: *Real and virtual nuclei in a transforming matrix*

We consider all possible nuclei in the crystal volume *V* during an interval *dt*: their number is given by $dn = NVdt$. Some of these "real" nuclei (*dnr)* form, while the other "virtual" nuclei *dnv* do not develop because they can overlap with other transformed volumes:

$$dn = dn_r + dn_v \tag{12.17}$$

Since every nucleus has the same volume during the interval *dt*, we can write:

$$\frac{dn_r}{dn} = \frac{dV_r}{dV} = \frac{dX_r}{dX} \tag{12.18}$$

where X_r and X represent the real and total nuclei volume fractions. Suppose $d\rho$ is the number of nuclei that form per unit volume during the time interval dt, $dnr = Vnt\, d\rho$, and $dn = Vd\rho$ where V_{nt} is the volume of the non-transformed phase.

Thus:

$$\frac{dX_r}{dX} = \frac{dn_r}{dn} = \frac{V_{nt}}{V} = \frac{V - V_t}{V} = 1 - X_r \tag{12.19}$$

By integrating (12.19), considering that $X(t = 0) = Xr\ (t = 0) = 0$, we get:

$$X_r = 1 - e^{-x} \tag{12.20}$$

Equation (12.16) implies that $X = \frac{\pi}{3} Iv^3 t^4$ and then:

$$X_r = 1 - e^{-\frac{\pi}{3} Iv^3 t^4} \tag{12.21}$$

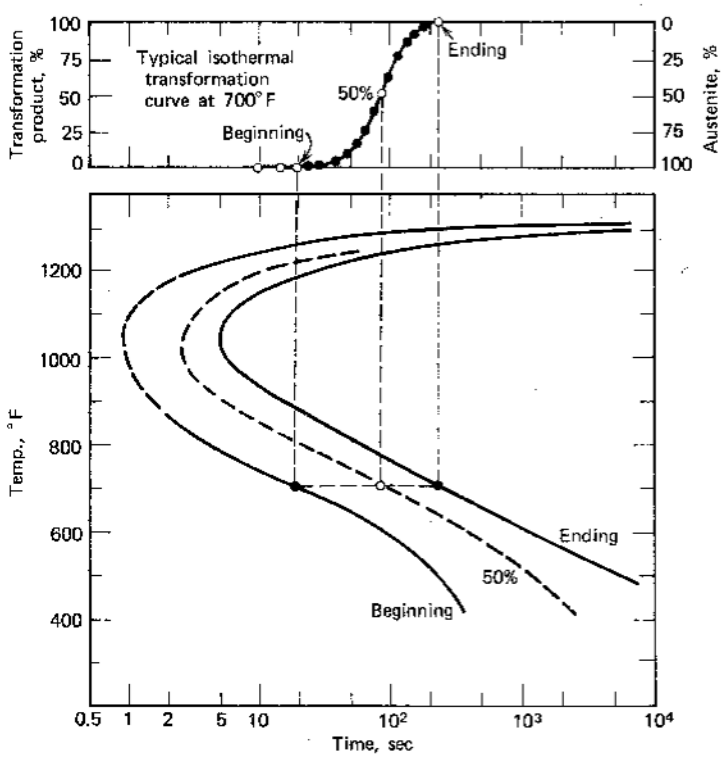

Figure 12-11: *Transformed phase in a TTT diagram according to Avrami kinetics*

Equation (12.21) is called the Johnson-Mehl equation. It is used in general under Avrami s and Kolmogorov's form:

$$f = 1 - e^{-kt^n} \tag{12.22}$$

where the exponent n (Avrami parameter) can vary between 1 and 4 and is related to the type and dimensionality of growth, e.g., an Avrami exponent of 4 corresponds to homogenous nucleation with 3-D growth (spherical particles). If the nucleation and growth mechanisms do not change, n is constant. On the other hand, the coefficient k depends on the nucleation and growth rates and is highly temperature-dependent. The Avrami equation is a semi-empirical relation. It enables us to calculate the transformed phase fraction at any point of a TTT diagram.

12.4 Examples of TTT diagrams

In the following diagram (Figure 12-12), we can observe the isothermal transformation of a steel alloy.

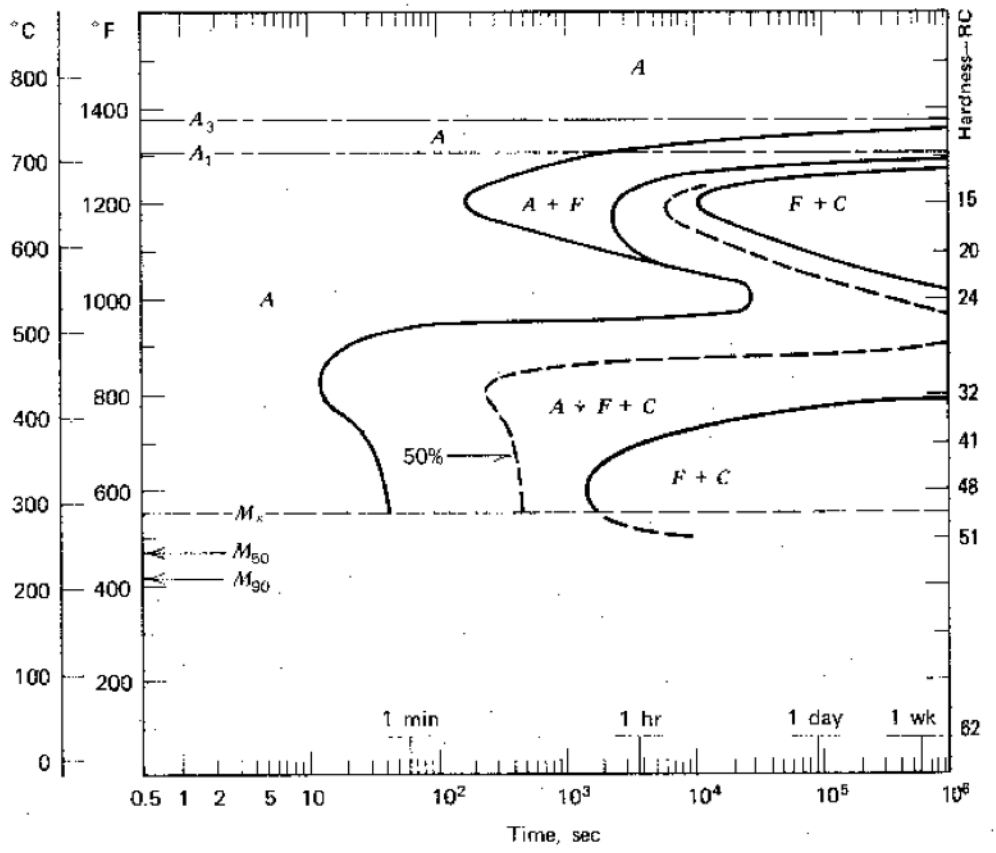

Figure 12-12: *TTT diagram of a steel alloy 4340: 0.42C, 0.78Mn, 1.79Ni, 0.8Cr*

The diagram in Figure (12-12) was obtained by quenching the steel in its austenitic state in a bath maintained at different temperatures. These curves can be generated by observing the microstructure at various times during the isothermal annealing. We can also measure resistivity, specific heat, or other parameters from which the phase change can be tracked. We note the presence of two noses" in the diagram, one corresponding to the transformation of austenite → pearlite and the other to bainite formation. These two structures are a mixture of ferrite and Fe_3C (F+C in Figure 12-12), although they have very different microstructures. Pearlite (see § 11.6.3) has a typical structure for a lamellar eutectic, while bainite microstructure morphologies are qualitatively different, comprising thin acicular carbides dispersed in a ferrite lamellar matrix. The transformation to pearlite is very slow, and new nuclei can develop ahead of the propagation. In bainite, ferrite grains nucleate and grow with a preferential orientation with respect to austenite grains. The bainite transformation occurs at a much lower temperature than conditions leading to pearlite formation. They require large undercoolings, and the transformation occurs almost instantaneously after the nucleation. At these lower temperatures, bainite forms more thin laths. Since the transformation kinetics at different cooling rates produce two distinct bainite morphologies, they are often referred to as upper and lower bainite (Figure 12-13). Upper bainite ferrite is free from carbides precipitating from the austenite phase between the ferrite plates. Lower bainite has a fine dispersion of plate-like carbides inside the ferrite plates.

The cooperative transformation of bainite introduces another kind of cooperative transformation, but without diffusion, the martensitic transformation. Martensitic phases form when steel is rapidly quenched below the line M_s. Under such rapid quenching, carbon atoms are trapped in the FCC lattice, producing a distortion that makes it tetragonal. We discuss these transformations in § 12.6.

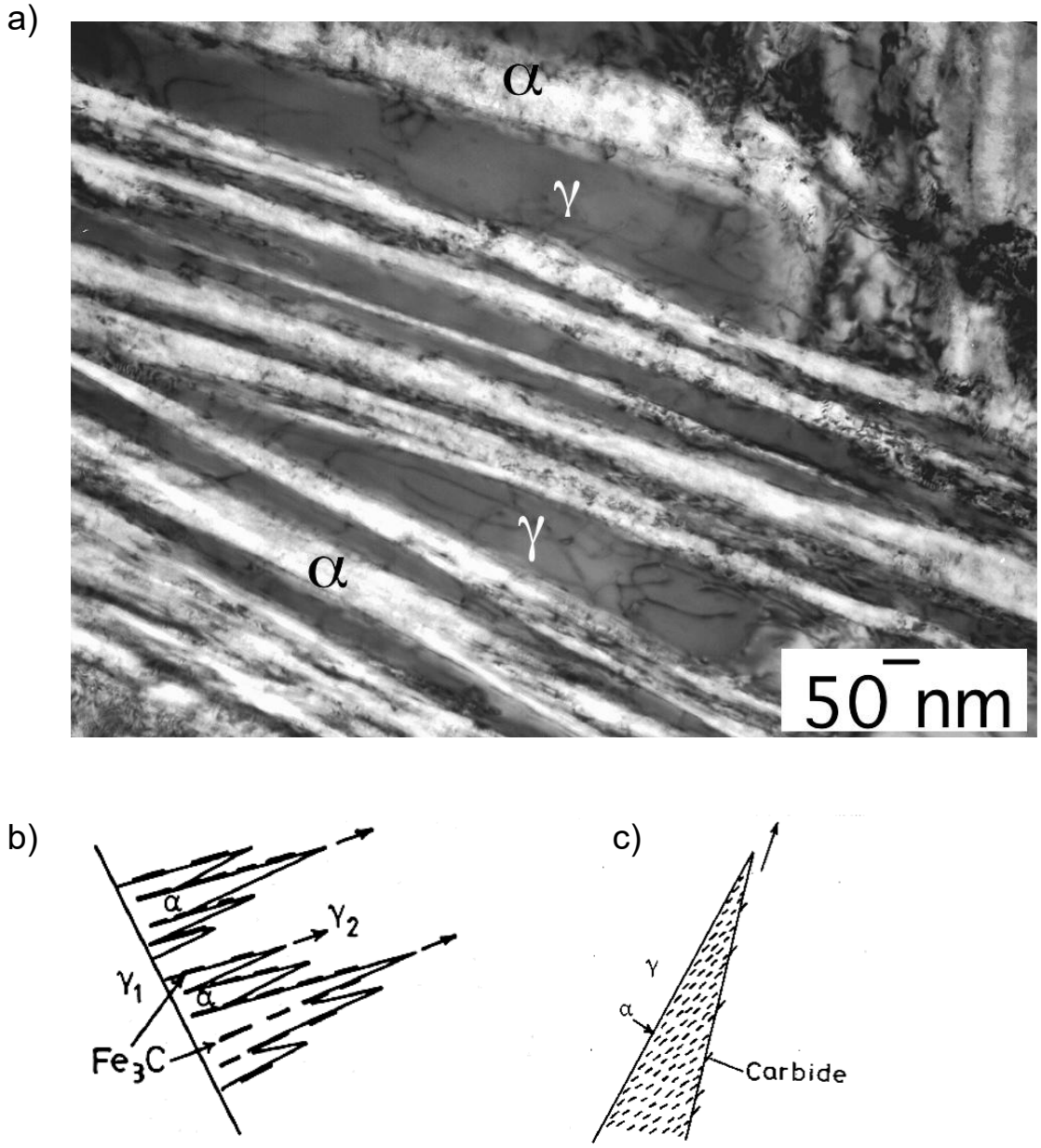

Figure 12-13: *a) Bainite platelets in austenite. b) Upper bainite structure (nucleation at a grain boundary). c) Lower Bainite structure*

12.4.1 CCT diagrams (Continuous cooling transformation)

The isothermal annealing process does not correspond to conditions achievable for thermal treatment. In general, we cannot control or know the cooling speed. The continuous cooling transformation curves (CCT diagrams) shown in Figures 12-14 describe the transformations during cooling from the austenite phase and allow engineers to empirically predict steel microstructure and hardness. The contour lines in these diagrams represent the phases that form during continuous cooling as a function of time and phase fraction for a given cooling speed. Experimentally, we can obtain these cooling

speeds by the Jominy bar test, in which a standard cylinder (bar) sample is partially quenched in a water bath on one end to create a gradient in cooling rates. The portion near the end is dipped into the water, resulting in the highest cooling rate. We can record the temperature changes during cooling along the length of the bar using thermocouples to measure the effective cooling rates. After the quenching step, the bar is sliced into sections along its length to observe the microstructure and the amount of phase present, and to measure its hardness (HRC = Rockwell C). These microstructure observations and hardness measurements are used to construct the empirical contours of the CCT curves. In steel samples, the highest quench rates produce a martensitic phase with higher hardness than the softer phases of bainite, ferrite, and pearlite.

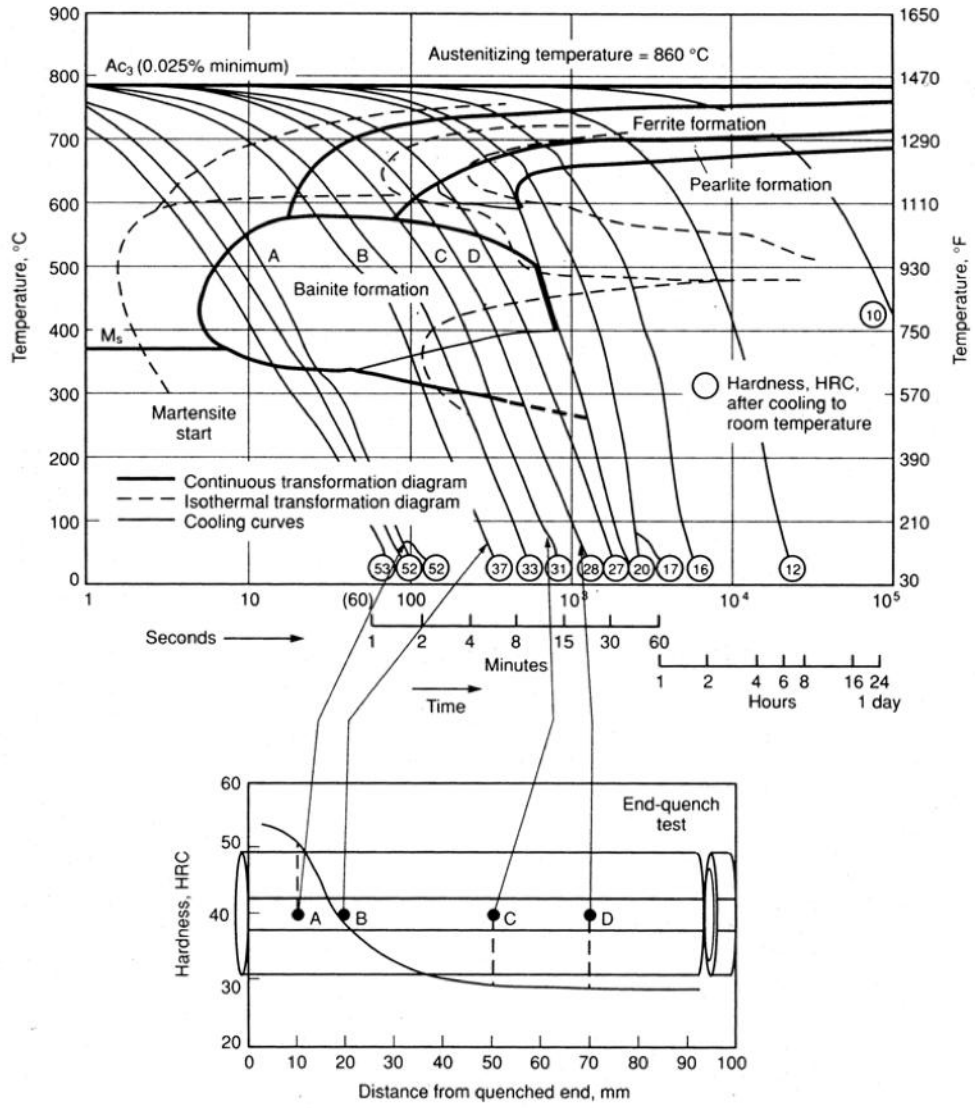

***Figure 12-14**: The CCT diagram is obtained via the quenching of a Jominy sample*

12.5 Transformations without diffusion

So far, we have considered transformations that imply compositional changes in the alloy, which need atomic diffusion over long distances, and diffusion is the primary driving mechanism supplying the growth of the new phase. Other solid-state transformations require only local atomic displacements

with distances shorter than interatomic spacing. Diffusion is unnecessary in those cases, or it can even act against the formation of a new phase if it is metastable. The martensitic phase transformation is the most technically significant among these diffusionless transformations. Martensitic microstructures provide both high strength and toughness. The scientific observations of martensite in the late 1800s and new methods for processing martensitic steels were primary technological advancements that brought the world into the modern age. These transformations are obtained through the coordinated local displacements of atoms in the crystal lattice. These displacements generally lead to a change in the unit-cell volume or the volume occupied by the atoms in the unit cell, and to a rearrangement of these atoms. Thus, a transformation with an expansion (Bain distortion) or deviation (invariant plane strain) occurs, according to which phenomenon is dominant. When no volume change occurs, a family of atoms has a coordinated shuffle within the cell (Figure 12-15) or produces a shear.

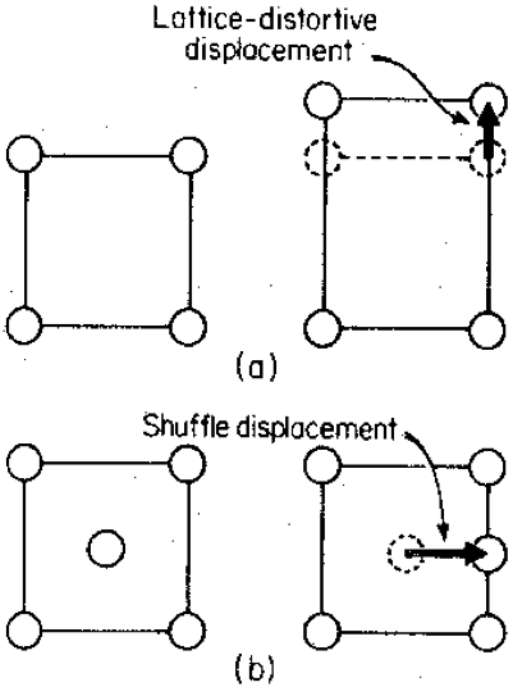

Figure 12-15: *Transformation with a dilatation (a) and with a deviation (b)*

12.6 The martensitic transformation

The martensitic transformation originates from one of the most important and widespread metallurgical processes: steel quenching. The empirical discovery of this process goes back many thousands of years, arising from the natural combination of iron with the carbon released by the embers left by the fires used to work iron. The oldest object showing a martensitic structure is a miner's pickaxe found in Galilee, dating back to the 12-13th century BC. In steel, martensite forms when carbon diffusion is prevented by rapid cooling of the FCC phase (austenite). The carbon solute in austenite is trapped in the α ferrite. The BCC structure of ferrite distorts, resulting in a metastable phase oversaturated with carbon and a body-centered tetragonal structure (BCT). This phase is called martensite, named after the Prussian researcher Martens, who first observed it in 1878.

12.6.1 Crystallography of the martensitic transformation

Bain was the first to research a crystallographic model of the martensitic transformation in 1924. His model is based on observations that an FCC structure at high temperatures transforms into a body-centered tetragonal lattice upon quenching (Figure 12-16). At low temperatures, the structure tends towards a BCC lattice but remains distorted. Without carbon interstitials, we expect a contraction of axis c and a dilatation of axes *a* and *b*. However, interstitial carbon atoms occupying octahedral sites in the FCC phase expand the c-axis, producing a body-centered tetragonal structure (Figure 12-16b). We correlate the amount of lattice distortion to the carbon content. The variation of *a* and *b* lattice constants to c-axis expansion (Figure 12-17) as a function of the carbon content follows this empirical equation:

$$\frac{c}{a} = 1.005 + 0.045(wt\%C) \tag{12.23}$$

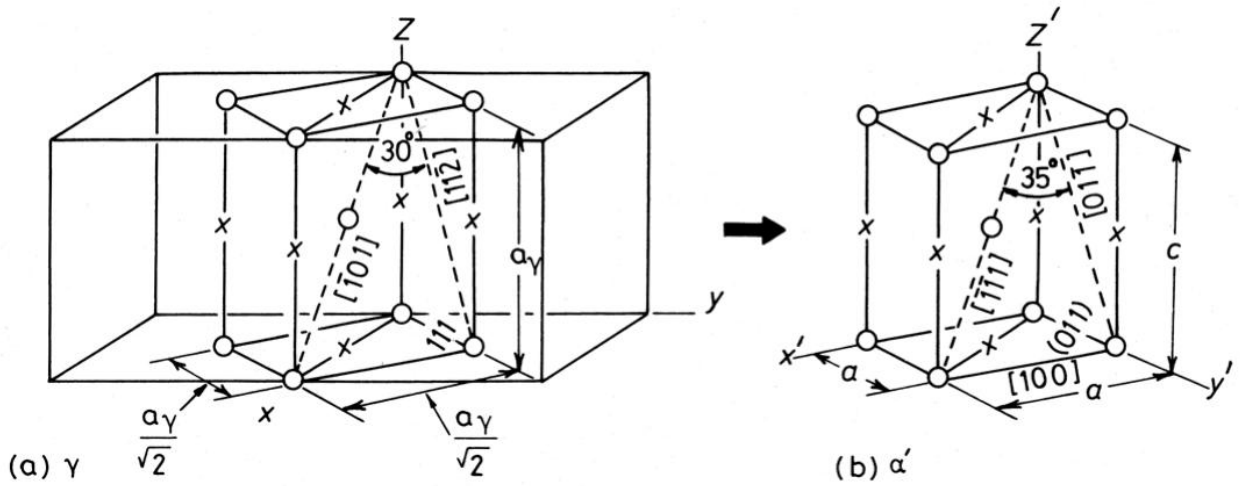

Figure 12-16: *Bain correspondence between FCC and BTC cells. The final tetragonal cell is obtained with a contraction by 18% of the Z axis and dilatation by 12% of the X and Y axes.*

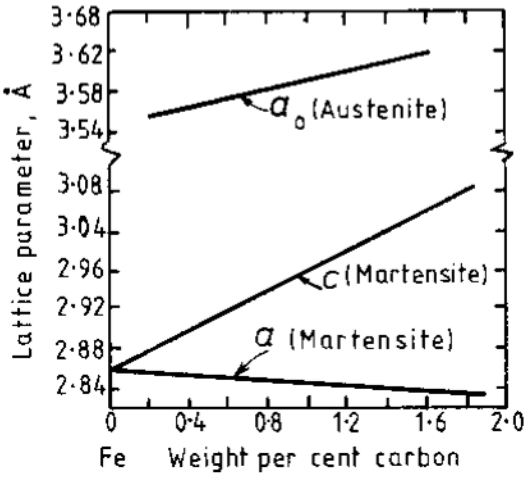

Figure 12-17: *Variation of the parameters a and c of the martensite tetragonal cell as a function of the carbon content*

The Bain transformation implies significant strains. If a martensite nucleus forms, it must overcome a significant potential barrier. However, the martensitic transformations occur practically without thermal activation, with propagation speeds of the front close to the speed of sound. Moreover, the interface with austenite remains coherent, with a clear continuity of the crystal planes. These observations imply that austenite and martensite must have a common interface invariant to this transformation. We call this interface the *habit plane*.

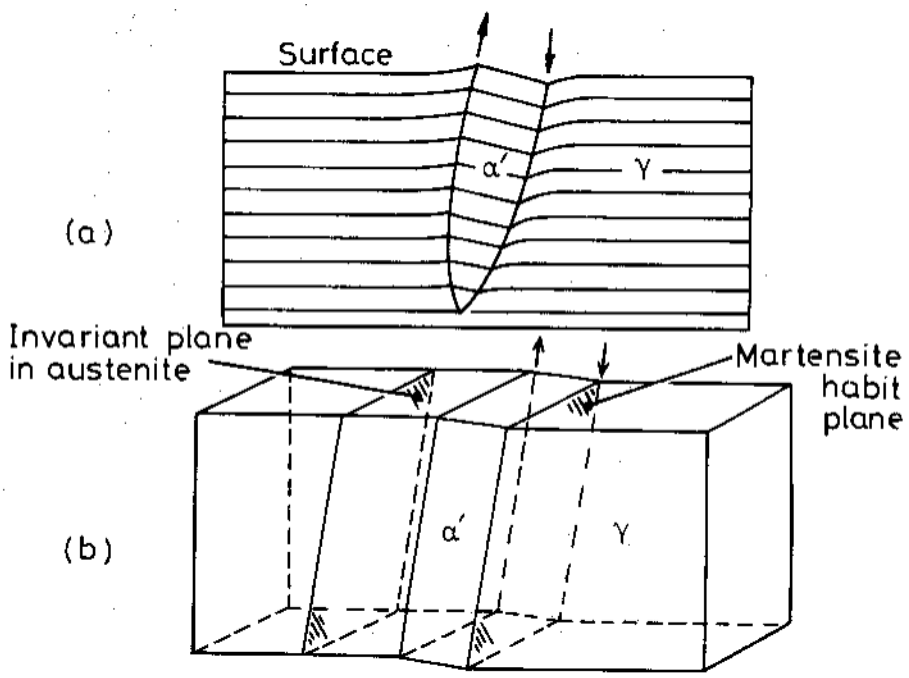

Figure 12-18: *The martensitic phase remains coherent with austenite. A bulge appears on the surface.*

We can give a geometrical representation of the Bain transformation by viewing it as an anisotropic affine deformation that maps a sphere into an ellipsoid in a continuous medium. The unit sphere represents the FCC structure, and the ellipsoid represents the BCT phase. We have a contraction of the Z-axis and a dilatation of the X- and Y-axes. As a result, two families of planes exist, AOC and BOD, which transform into the planes A OC and B OD,' with the vectors parallel to the plane ZY that remain invariant. The vectors (crystal directions) that form the AOB and DOC cones contract during the Bain transformation, whereas those for AOD and BOC expand. The Bain transformation does not have an invariant plane with the two lattices, but only lines, those lines that define these cones. This new strain expands the X-axis and is needed to construct planes invariant to the transformation. As theoretically explained, for samples deformed by compression or traction from the motion of dislocations that shear the crystal, we offset the expansion in X by a suitable choice of the atomic glide planes. Figure 12-20 illustrates the shear (via a twinning deformation) geometry producing the transformation with invariant habit planes. As before, a family of planes (K_2) is invariant to shear deformation. The vectors located in the planes on the left of the K_2 contract and those on the right expand. The second invariant direction is given by a vector belonging to the plane AOC chosen previously, which gives the contraction (or expansion) in the X-axis direction. This can potentially introduce further deformation in the ZY plane, which is offset by modifying the choice of the plane AOC (Figure 12-21).

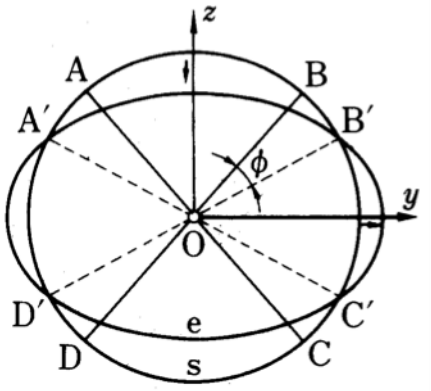

Figure 12-19: *Strain of the FCC lattice according to Bain transformation. We notice a contraction of the Z-axis and an expansion of the X and Y axes. Two families of planes, AOC and BOD, have invariant projected distances on Z and Y. e=ellipse s=sphere.*

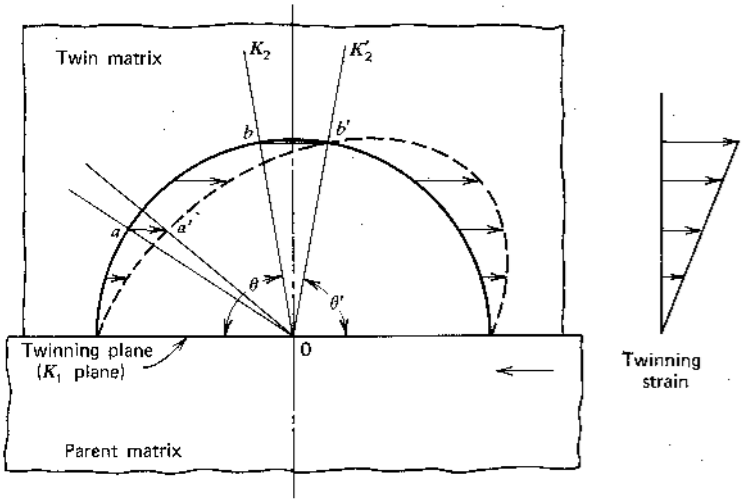

Figure 12-20: *Shear on a plane called K1 in the direction d. The plane K2 is invariant*

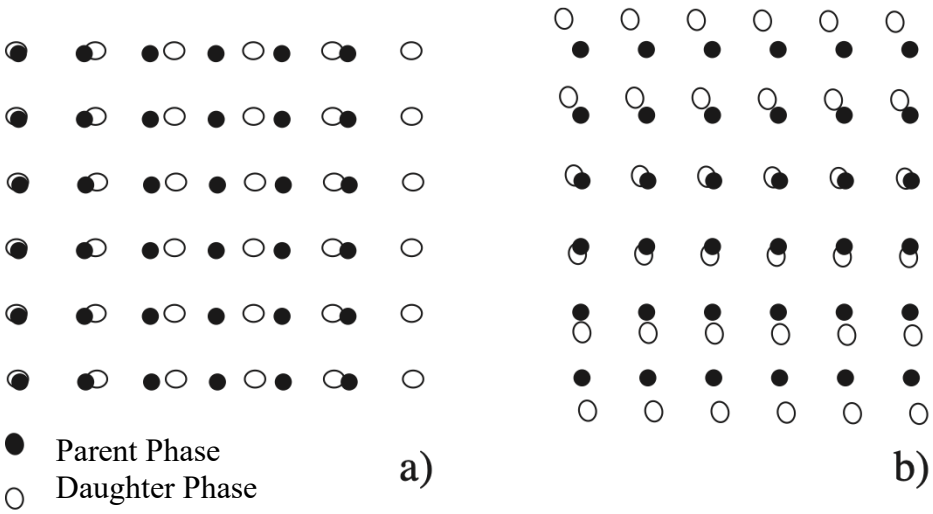

Figure 12-21: *Shear example. The planes of the daughter phase are expanded in the direction of X compared to the parent phase (a). A shear by an angle of 20˚ on an inclined line at 45˚ offsets the expansion but also produces an expansion along the Z axis (b)*

Generally, there is a more effective way to generate an invariant shear. This procedure is called twinning. Twinned crystals have mirror symmetry or a 180˚ rotation. If we consider Figures 12-20, the invariant planes K_2 and K'_2 provide the symmetry planes of the twins. However, crystal twinning does not correspond to a rotation of the atoms by 180˚. The metaphor of mirror symmetries corresponds only to the crystallographic structure. The actual displacement of each atom is less than an interatomic distance. As such, the martensitic transformation proceeds quickly, reaching the speed of sound in the material.

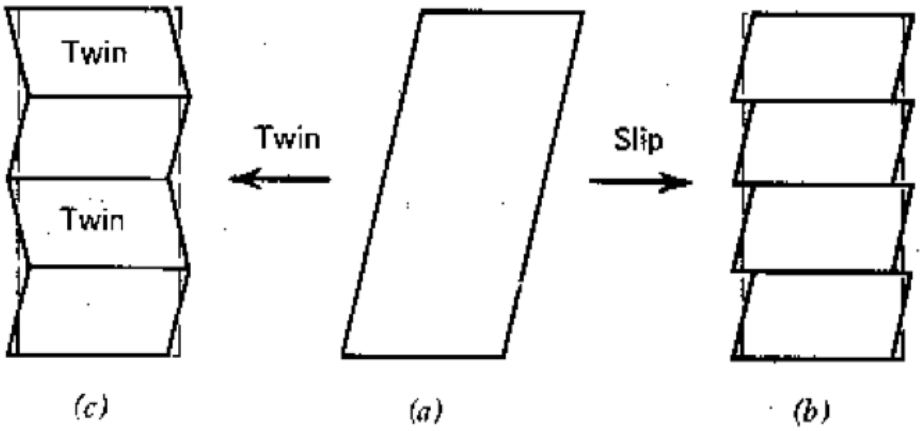

Figure 12-22: *The shear or twinning can reduce the distortion between austenite and martensite considerably*

In short, the operations required to obtain a strain that preserves an invariant plane of the lattice comprise three operations:

1) Distortion (Bain) to generate the new lattice symmetry,
2) Shear leaves the cell untouched. This shear acts on the natural glide or twinning planes of the martensite,
3) Rotation of the martensitic lattice to the new lattice in correspondence with the habit plane.

The sequence of these operations can be represented mathematically by the multiplication of the three corresponding transformation matrices:

$$P=RSB \tag{12.24}$$

where B represents the Bain distortion in the volume, S is the twinning shear, and R *is* the rigid body rotation needed for lattice correspondence to the habit plane.

12.6.2 Thermodynamics of the martensitic transformation

Several alloys exhibit martensitic transformations. As in all phase transformations, a specific potential barrier must be overcome to form a nucleus of the new phase. The nucleus of the new phase can be assumed to have a flat, lenticular shape, a reasonable assumption based on experimental microscopy observations showing martensite with long platelet morphologies (12-23).

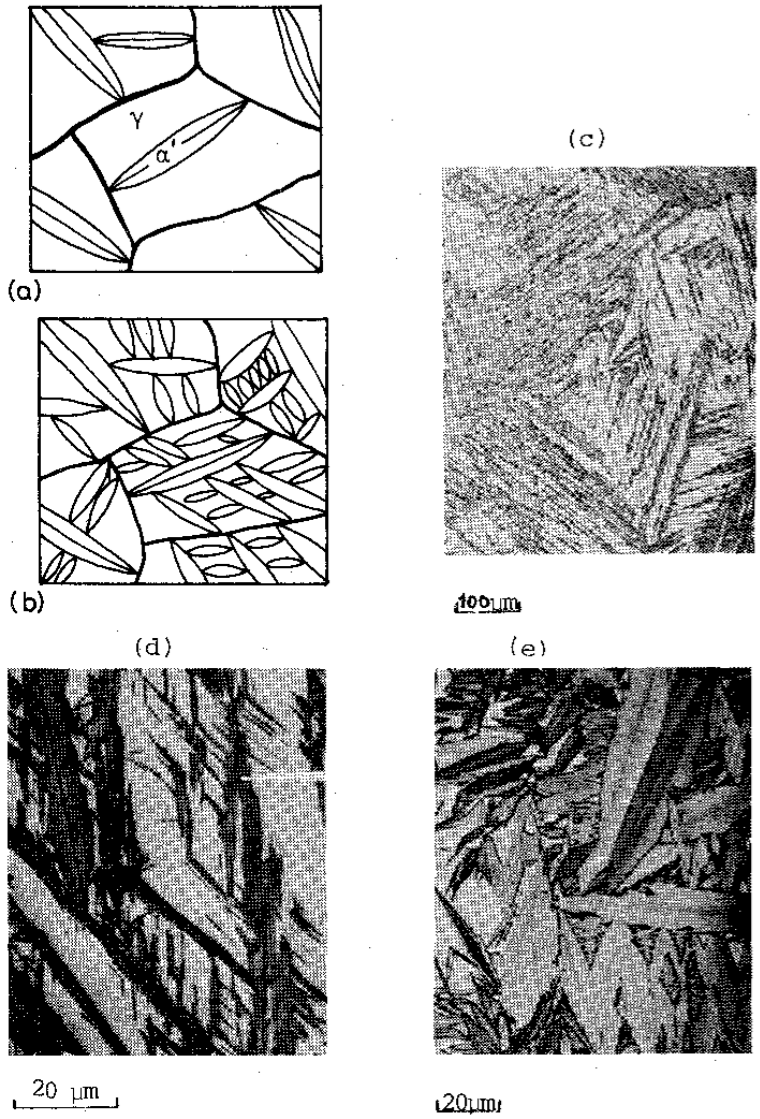

Figure 12-23: *Formation of platelets of martensite in Fe-Ni. a) b) Formation mechanism of the platelets. They can end on a grain boundary or another platelet. Comparison between the structure in laths c) and the structure in platelets d) e)*

The energy variation associated with the formation of the active nuclei is given by (see equation 12.1):

$$\Delta G = V(\Delta g_V + \Delta g_{el}) + S\gamma$$

Considering nuclei with elliptic shapes, we can show by using Eshelby's theory (J.W. Christian, *The Theory of Transformations in Crystals*, Pergamon, 1965) that the elastic energy per unit volume is given by

$$\Delta g_{el} = 2\mu\left(f_1(v)(\varepsilon_{11})^2 + f_2(v)(\varepsilon_{12})^2 \cdot \frac{c}{a} \right) \qquad (12.25)$$

$f_1(v)$ and $f_2(v)$ are functions of the Poisson ratio, *c* and *a* are the minor and major semiaxis of the ellipse, respectively, and ε_{11} and ε_{12} are the average dilatation and shear strains, respectively.
Considering that, in general, in martensitic transformations, the volumetric strain ε_{11} is negligible compared to the shear ε_{12}, we can write that $\Delta g_{el} = A \cdot \frac{c}{a}$, where *A* is a function of the elastic constants. Equation (12.1) becomes:

$$\Delta G = \frac{4\pi}{3} a^2 c \Delta g_V + \frac{4\pi}{3} a c^2 A + 2\pi a^2 \gamma \tag{12.26}$$

As in the case of transformations with diffusion, the propagation of the new phase is inhibited by the elastic and surface energies stored in it. Thus, the chemical energy must be sufficiently large. As already seen in § 11.4.1, the transformation is done at a lower temperature (M_s for Martensite start") than the equilibrium temperature between the two phases. The chemical energy necessary for the transformation is given by (11.35):

$$\Delta g_V = \Delta s_T \Delta T$$

where $\Delta s_T = \frac{\Delta h_T}{T_E}$ is related to the latent heat of the transformation Δh_T.

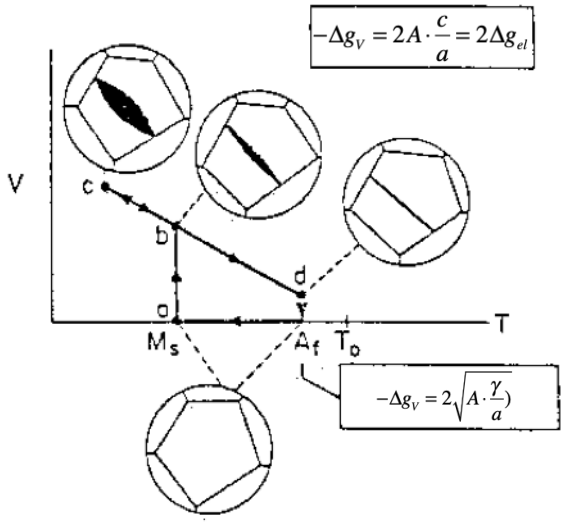

Figure 12-24: *Transformation of a platelet of martensite in two phases: 1 - the instantaneous extension of the radius of the platelet until it reaches the grain boundary, 2 - increase of the thickness at elastic equilibrium*

For an elliptical nucleus, the transformation can be represented by the diagram in Figure 12-24. We suppose a newly-formed nucleus grows until it intersects the austenite grain boundary. The thickness increases at equilibrium with the elastic stresses. By differentiating (12.26) with respect to *c*, we get the equilibrium condition:

$$-\Delta g_V = 2A \cdot \frac{c}{a} = 2\Delta g_{el} \tag{12.27}$$

If we continue the heating cycle, the platelet of martensite remains in equilibrium with austenite until a temperature A_f (Austenite final") is given by the condition $-\frac{\partial \Delta G}{\partial a}=0$, under the constraint given by (12.27). We obtain:

$$-\Delta g_V = 2\sqrt{A \cdot \frac{\gamma}{a}}) \tag{12.28}$$

Stated in another way, acquiring a specific thickness stabilizes the platelet beyond M_s. The cycle of martensite's appearance and disappearance shows some hysteresis. The hysteresis amplitude allows us to distinguish two types of behavior during martensite formation. The hysteresis ranges from 400 K to more in alloys such as Fe-C and Fe-Ni; other alloys, such as Au-Cd and Ti-Ni, exhibit hysteresis of about tens of degrees. The strain amplitude associated with the phase transformation explains these hysteresis values. The way the two kinds of martensite form is profoundly different. The strains in martensitic materials with high hysteresis are so large that martensite growth causes austenite's plastic deformation. The coherence of the interface is thus destroyed, and the martensite plate cannot grow beyond a specific size. The further development of martensite can only occur through the nucleation of new platelets. In such martensitic transformations, the interface energy term is dominant.

For martensitic materials with low hysteresis (*thermoelastic*), a platelet grows in elastic equilibrium with the matrix until it reaches the physical boundaries with other platelets or austenite grain boundaries. Thus, heating thermoelastic martensite causes the same platelets to shrink and reform austenite again (Figure 12-24). In nonthermoelastic martensite, austenite also grows by nucleation-growth in martensite, in which some amount of elastic energy is required to create a nucleus of austenite. This fact explains the large amplitude of the hysteresis.

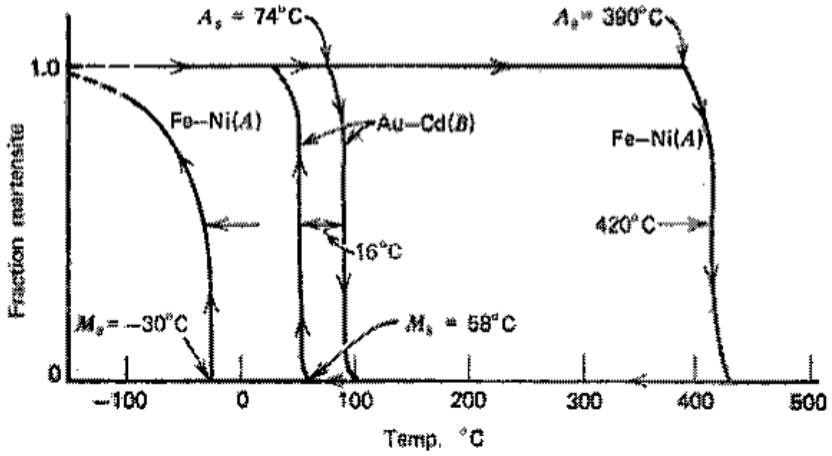

Figure 12-25: *Hysteresis cycle in two martensitic alloys: Fe-Ni and Au-Cd*

Remark

When heated, Martensite in Fe-C alloys loses its beneficial mechanical properties because carbon diffuses, leading to carbide precipitation and a reduction in strength. The reduced strength results from martensitic lattice structural changes that become more similar to those of α ferrite. Thus, the transformation by heating occurs primarily from ferrite to austenite, with austenite developing by nucleation and growth.

12.7 Thermoelastic alloys: Shape Memory Effect and Pseudoelasticity

12.7.1 Shape memory effect

Thermoelastic alloys are particularly interesting for practical applications due to their remarkable mechanical behavior. For example, the stress field determines the equilibrium of a martensite platelet in its surroundings: it develops at an equilibrium between chemical and elastic energy. Therefore, the local field is modified when an external stress is applied, leading to a different configuration of martensite platelets. When thermoelastic martensite is deformed, the strain occurs by the propagation of twin boundaries through the movement of partial dislocations, similar to those created for stacking faults. Under applied stress, twinning dislocations with the highest Schmid factor move to twin or detwin (un-shear) the crystal (Figures 12-26(c) and (d)). While a net shape change occurs, no volume change occurs as dislocations are not created nor annihilated during this type of twin boundary motion. Only those coherent twin boundaries produced by the martensitic transformation move and induce the strain. As such, those strains can be fully recovered upon heating and transforming back to the austenite phase.

All the twins in a martensite platelet form from a single austenite crystal. Thus, during heating, regardless of the deformed phase configuration, the martensite reverts to the austenite parent phase's initial structure. As a result, the material recovers its original macroscopic shape. Suppose the martensite deformation is so large that it creates dislocations or causes the glide of existing perfect dislocations not associated with the martensite twin; a permanent, unrecoverable strain results. In materials such as TiNi alloys, up to 10% of the plastic deformation associated with twin boundary motion can be recovered through this shape memory effect. Applications of this effect include dental appliances, medical probes, opening solar panels in space, etc.

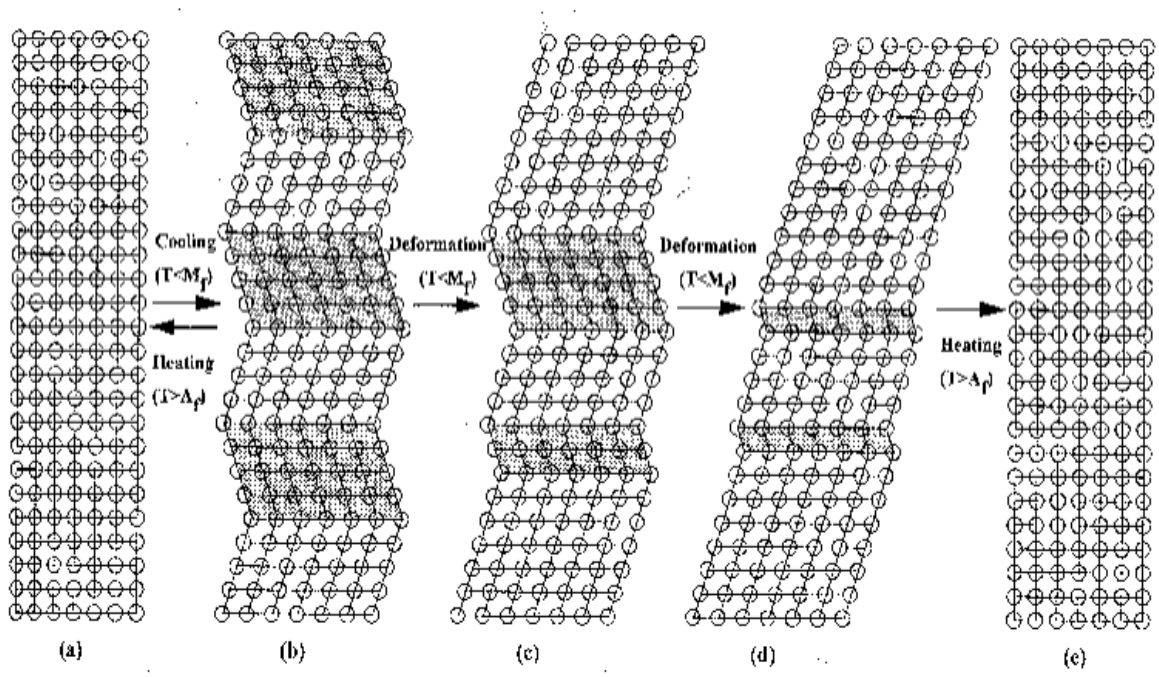

Figure 12-26: *Mechanism of the memory effect. During the deformation, one type of twin converts into another. During heating, all the twins return to the austenite grain orientation that generated them.*

12.7.2 Pseudoelasticity

Figure 12-27 shows the strain-stress curves of a Cu-34%Zn-3%Sn measured at different temperatures. We note that, beyond the temperature A_S, even though strains exceed the elastic limit and result in large plastic deformations in most metal alloys, the CuZnSn sample recovers its initial shape either at the end of the cycle (244 K) or after a slight relaxation of the flow stress (297 K). The material exhibits "rubber-like behavior" (pseudoelasticity) and superelasticity, linked to the peculiar nature of martensite.

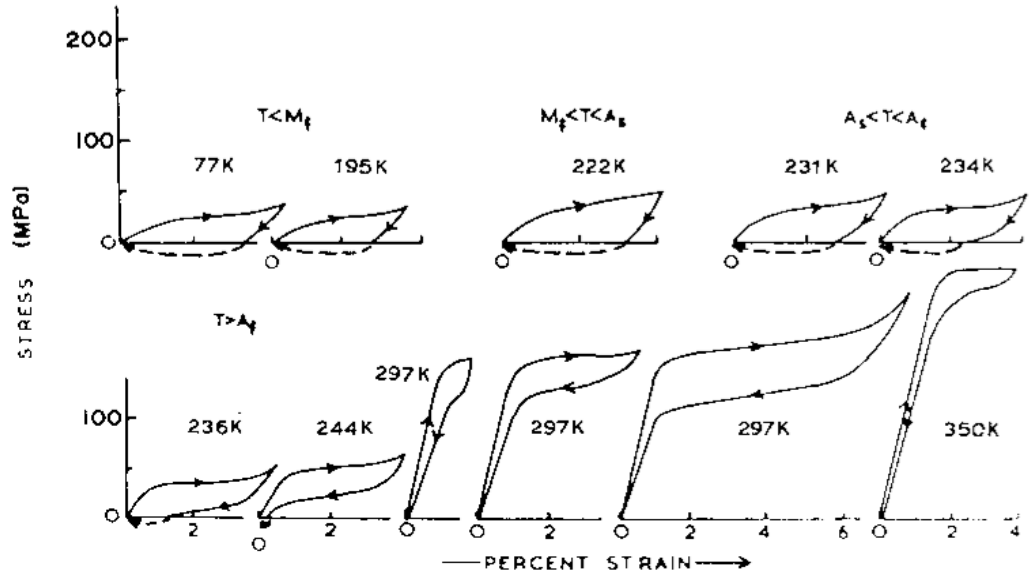

***Figure 12-27**: Tensile test curves of an alloy Cu-34%Zn-3%Sn. Ms =221 K, Mf =208 K, As =223 K, Af =235 K.*

In this "rubber-like" behavior, the motion of twin boundaries is fully reversible upon releasing the applied stress, unlike the recovery process in shape memory effect mechanisms. The physical origins of such behavior are not yet evident. However, the behavior is related to the development of internal elastic stresses during deformation, which cause the twins formed under stress to revert to the original twin structure.

This superelastic behavior is observed above the austenite finish temperature (A_f). Martensite is thus a thermodynamically unstable phase. However, under applied stress, austenite transformed into martensite. When the stress is released, the thermodynamic situation changes again, and martensite becomes unstable. The induced plastic deformation associated with the thermoelastic transformation to martensite is then recovered. This material under applied stress exhibits apparent plastic behavior, with almost ideal plasticity beyond the elastic yield strength. As stress decreases, the material regains its restoring force and eventually returns to its original shape. The superelastic strains can reach 20%. Applications of pseudoelasticity include, for example, aerospace couplings, medical appliances and probes, eyeglasses with reversible deformation frames, and bra reinforcements.